Supplemental Material: Shock-driven amorphization and melt in Fe_2O_3

Céline Crépisson,[1,*] Alexis Amouretti,[2,3] Marion Harmand,[2,4] Chrystèle Sanloup,[5] Patrick Heighway,[1] Sam Azadi,[1] David McGonegle,[6] Thomas Campbell,[1] Juan Pintor,[2] David Alexander Chin,[7] Ethan Smith,[7] Linda Hansen,[7] Alessandro Forte,[1] Thomas Gawne,[1] Hae Ja Lee,[8] Bob Nagler,[8] YuanFeng Shi,[1] Guillaume Fiquet,[2] François Guyot,[2] Mikako Makita,[9] Alessandra Benuzzi-Mounaix,[10] Tommaso Vinci,[10] Kohei Miyanishi,[11] Norimasa Ozaki,[3,12] Tatiana Pikuz,[3] Hirotaka Nakamura,[3] Keiichi Sueda,[11] Toshinori Yabuuchi,[11,13] Makina Yabashi,[11,13] Justin S. Wark,[1] Danae N. Polsin,[7] and Sam M. Vinko[1,14]

[1]*Department of Physics, Clarendon Laboratory, University of Oxford, Parks Road, Oxford OX1 3PU, UK*
[2]*Sorbonne Université, CNRS, Muséum National d'Histoire Naturelle, Institut de Minéralogie,*
de Physique des matériaux et de Cosmochimie, UMR7590, Paris, France
[3]*Graduate School of Engineering, Osaka University, Suita, Osaka 565-0871, Japan*
[4]*PIMM, Arts et Metiers Institute of Technology, CNRS, Cnam,*
HESAM University, 151 boulevard de l'Hôpital, 75013 Paris, France
[5]*Sorbonne Université, CNRS, Muséum National d'Histoire Naturelle,*
Institut de Minéralogie, de Physique des matériaux et de Cosmochimie,
UMR7590, Institut Universitaire de France (IUF), Paris, France
[6]*AWE, Aldermaston, Reading, RG7 4PR, United Kingdom*
[7]*University of Rochester Laboratory for Laser Energetics, Rochester, NY, USA*
[8]*SLAC National Accelerator Laboratory, 2575 Sand Hill Rd, Menlo Park, CA 94025, USA*
[9]*European XFEL, GmbH, 22869 Schenefeld, Germany*
[10]*LULI, École Polytechnique, CNRS, CEA, UPMC, Palaiseau, FRANCE*
[11]*RIKEN SPring-8 Center, Hyogo 679-5148, Japan*
[12]*Institute of Laser Engineering, Osaka University, Suita, Osaka 565-0871, Japan*
[13]*Japan Synchrotron Radiation Research Institute, Hyogo 679-5198, Japan*
[14]*Central Laser Facility, STFC Rutherford Appleton Laboratory, Didcot OX11 0QX, UK*

(Dated: January 10, 2025)

I. EXPERIMENTAL SET-UP AND TARGETS

In-situ x-ray diffraction on shock-compressed Fe_2O_3 was performed using two different geometries. Data in transmission geometry were acquired during one experiment at MEC, LCLS and will be referred in the present supplementary material as LCLS data. Details of the experimental set-up is shown in Fig. S1. Data in reflection geometry were acquired during two experiments at BL3, SACLA and will be referred in the present Supplemental Material as SACLA1 and SACLA2 data. Only one data point was acquired during SACLA2 experiment at 182(6) GPa, while other data in reflection were acquired during SACLA1 experiment. Details of the experimental set-up is shown in Fig. S2.

We used two types of targets referred as CH-target and Sa-target. CH-targets were obtained by depositing 7 (SACLA1), 8 (LCLS) or 10 µm (SACLA2) Fe_2O_3 on top of a 54.3 (SACLA1), 62 (SACLA2) or 54 µm (LCLS) CH plastic parylene-N ablator. Sa-targets were obtained by depositing 8 µm Fe_2O_3 on top of a monocrystalline 22 µm thick sapphire window, a layer of 39 (SACLA1) or 54 µm (LCLS) parylene-N was then deposited on the other side of the Fe_2O_3 layer. For each type of target used in each experiment, we show the x-ray diffraction pattern of the starting material in Fig. S3.

---

[*] celine.crepisson@physics.ox.ac.uk

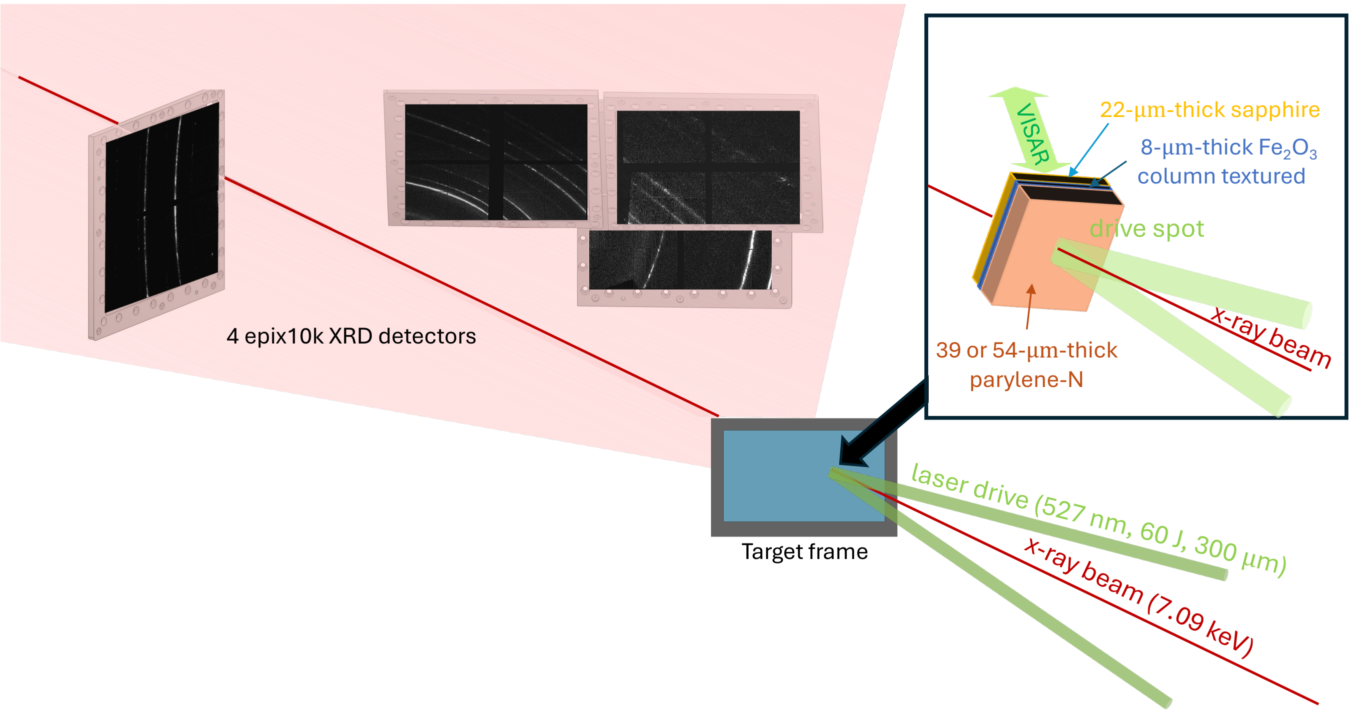

Figure S1. **Experimental set-up for data acquired in transmission geometry (LCLS data).**

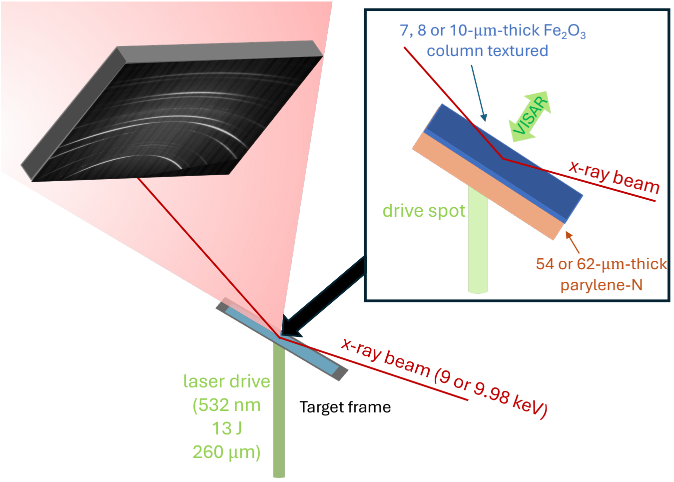

Figure S2. **Experimental set-up for data acquired in reflection geometry (SACLA1 and SACLA2 data).**

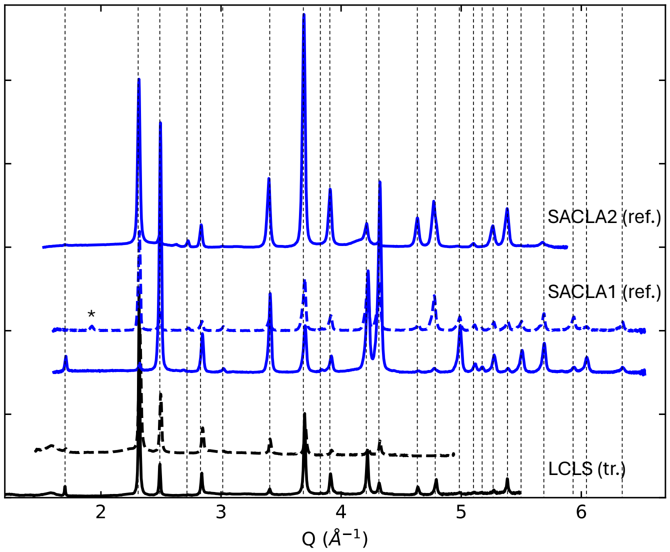

Figure S3. **x-ray diffraction measurements on Fe_2O_3 prior to shock.** Starting material for data acquired in transmission (tr.) referred as LCLS data (in black) and data acquired in reflection (ref.) referred as SACLA1 and SACLA2 (in blue). Sa-targets are shown in dashed-line and CH-target in plain line. α-Fe_2O_3 peaks are indexed (vertical dashed lines) [1]. For Sa-target, LCLS data, only one detector could be used for this particular run, explaining the low Q-range. * indicates a background peak also present at 209 GPa under shock for Sa-target SACLA1 displayed in Fig. 1 of the main paper, proving that it is coming from the background and not affecting the target.

II. VISAR ANALYSIS AND PRESSURE ESTIMATE

VISAR measurements were used to determine breakout time, i.e. the moment when the shock leaves the Fe_2O_3 layer, and velocity history. For data acquired in transmission (LCLS data) VISAR sensitivities are 4.5241 km/s fringes^{-1} and 1.9890 km/s fringes^{-1} and acquisition windows are 10 ns and 20 ns. Regarding data acquired in reflection : for SACLA1 data, VISAR sensitivities are 8.5297 km/s and 5.375 km/s fringes^{-1} and acquisition windows are both 10 ns. For SACLA2 data VISAR sensitivities are 5.375 km/s fringes^{-1} and 2.157 km/s fringes^{-1} and acquisition windows are both 20 ns. To determine pressure for Sa-target, particle velocity $u_p(Sa)$ was extracted from the Fe_2O_3/Sapphire interface by VISAR, further details being already described in reference [2]. The error on $u_p(Sa)$ is set as $\delta u_p(Sa) = 0.05 * (minimalVISARsensitivity)/n_0$ with n_0 the refractive index of sapphire at the VISAR wavelength. For example, for LCLS data $\delta u_p(Sa) = 0.06$ km/s. If the two velocities extracted from both VISAR were too different, we used the absolute difference between these two velocity values as uncertainty. Pressure and its uncertainty were then determined from u_p and δu_p by using Fe_2O_3 Hugoniot relations [3]. For all experiments, only breakout time could be measured for CH-targets under shock due to loss of reflectivity of the sample preventing any velocity determination. For LCLS data, we used breakout time versus pressure relationship obtained by interpolating available data measured on Sa-targets as shown in Fig. S4. For SACLA1 and SACLA2 data on Sa-targets were too few to be interpolated and hydrodynamic simulations were performed using code MULTI [4]. For SACLA1 hydrodynamic simulations using code MULTI [4] were performed in order to match the breakout time evaluated by VISAR analysis. For one data point upon release after a shock at 200(5) GPa (section V) VISAR data could not give a reliable breakout estimate: in this case a corrective factor between numerical and experimental intensity based on the other runs, was used. For SACLA2 hydrodynamic simulations were calibrated on a lower pressure run whose pressure was evaluated by VISAR analysis as shown in Fig. S5.

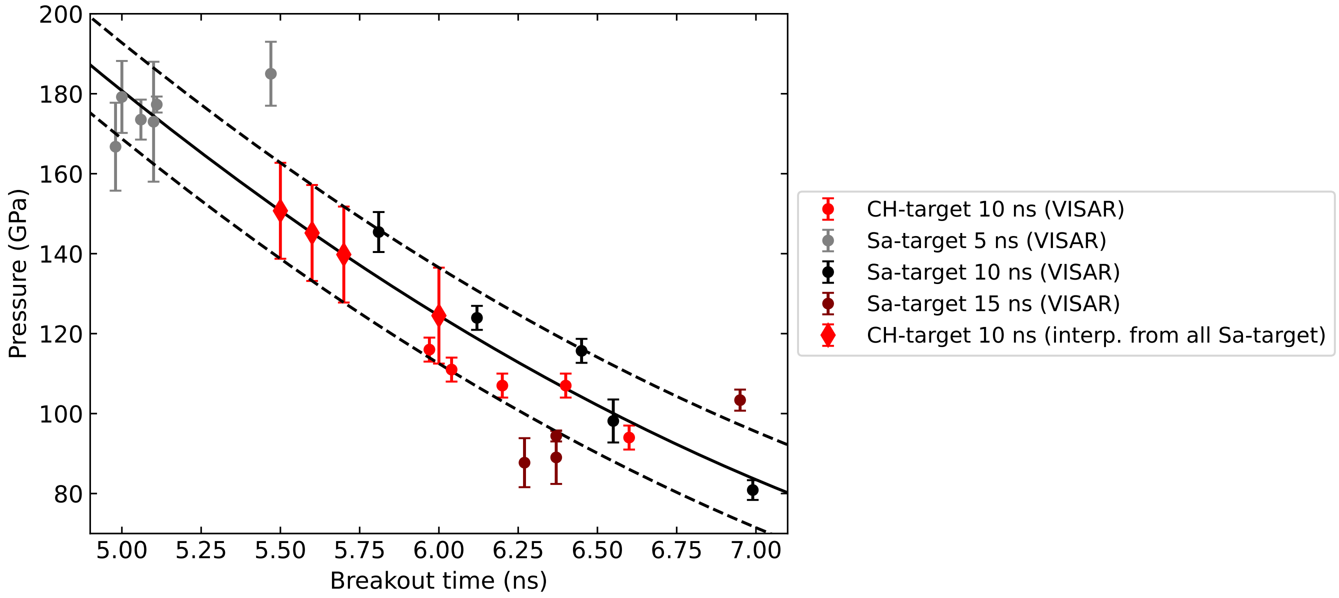

Figure S4. **Pressure determination for CH-targets (without window) for data acquired in transmission (LCLS data).** Relationship between the pressure and the time at which the shock leaves the Fe_2O_3 (breakout time). Pressure is determined from VISAR analysis for Sa-target. Pressure – breakout time relationship was interpolated (interp.) for Sa-targets with a second order polynomial and used to calculate pressure for CH-targets whose VISAR analysis is not feasible due to loss of reflectivity with amorphization of the sample. We note that dispersion is increased by the use of run with different pulse durations, possibly linked to variation in pulse profiles. To assess the goodness of the fit we show CH-target data points analyzed with VISAR (at lower pressure). We determine the error-bars for CH-targets so that all CH-targets analyzed with VISAR and all Sa-target runs with 10 ns pulse duration are within the fit-plus-error bars : this is achieved for an error bar of 12 GPa.

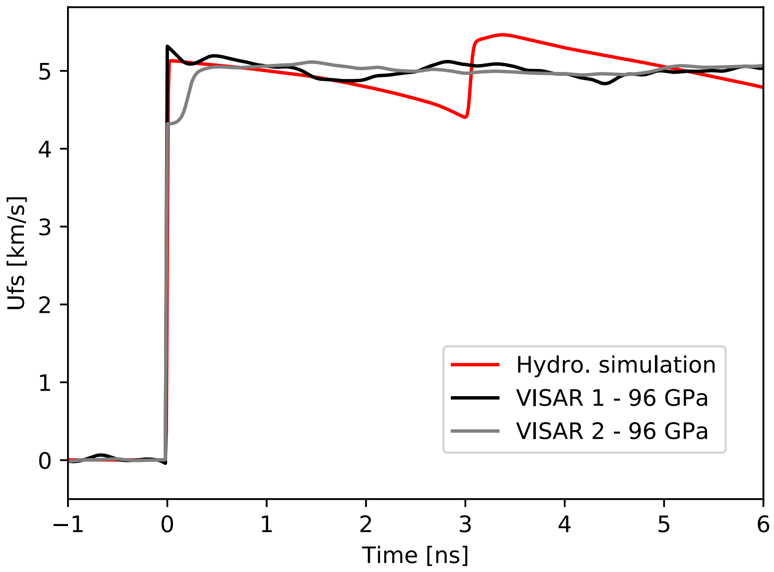

Figure S5. **Pressure determination for CH-targets (without window) for data acquired in reflection (here SACLA2 data).** Data point at 96 GPa on similar CH-target was analyzed by VISAR (at this pressure Fe_2O_3 is still reflective): free surface velocity was determined and assumed to be twice the particle velocity [5]. Using Rankine Hugoniot relations for Fe_2O_3 [3] a pressure of 96 GPa was determined. Hydrodynamic simulation using code MULTI [4] is shown to match the velocity profile for this run. Corrective factor between numerical (I_{num}) and experimental intensity (I_{exp}) was determined ($I_{num} = 0.68$ x I_{exp}). This correction was then applied for high pressure Fe_2O_3 from SACLA2 experiment with $I_{exp} = 4.37\text{e}12$ W/cm^2. Hydrodynamic simulation gave a pressure of 182(6) GPa. The uncertainty on this pressure is obtain from the propagation of free surface velocity (U_{fs}) uncertainty of the run at 96 GPa ($U_{fs} = 5.0$ +/- 0.1 km/s).

III. 2D DIFFRACTION IMAGE PLATE

Examples of 2D image plate for data acquired in transmission (LCLS data) and in reflection (SACLA1 data and SACLA2 for data point at 182(6) GPa) geometries are shown in Fig. S6 and Fig. S7.

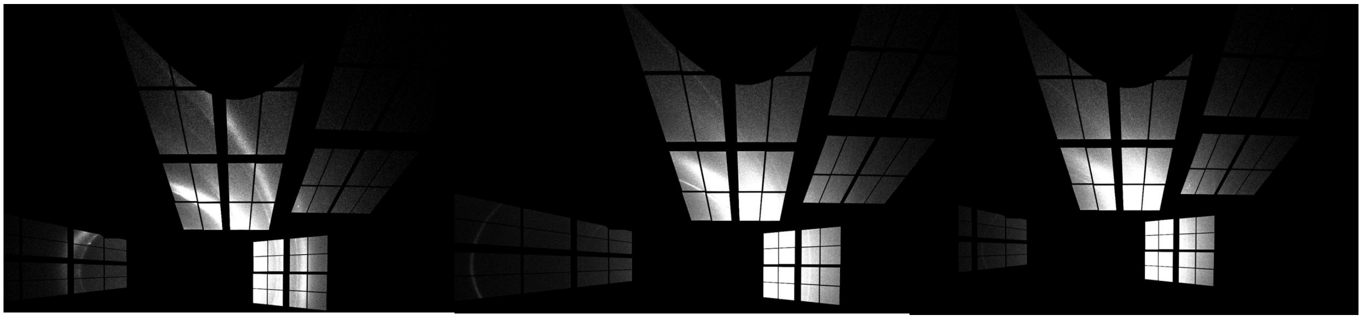

crystal (+amb. peaks)
47(2) GPa

diffuse feat. (+amb. peaks)
140(12) GPa

diffuse feat.(+amb. peaks)
151(12) GPa

Figure S6. **2D diffraction image plate for data acquired in transmission (LCLS data).** 2D image plate of crystalline α-Fe_2O_3 at 47(2) GPa from reference [2], of amorphous Fe_2O_3 at 140(12) GPa and of liquid Fe_2O_3 at 151(12) GPa showing both diffuse features (feat.) with remaining ambient (amb.) peaks. X-rays energy is 7.09 keV. Angular range is 20 to 100° scattering angle and azimuthal range is approximately 90 to 220° for the 3 detectors at the top and 0 to 60° for the detector at the bottom. .

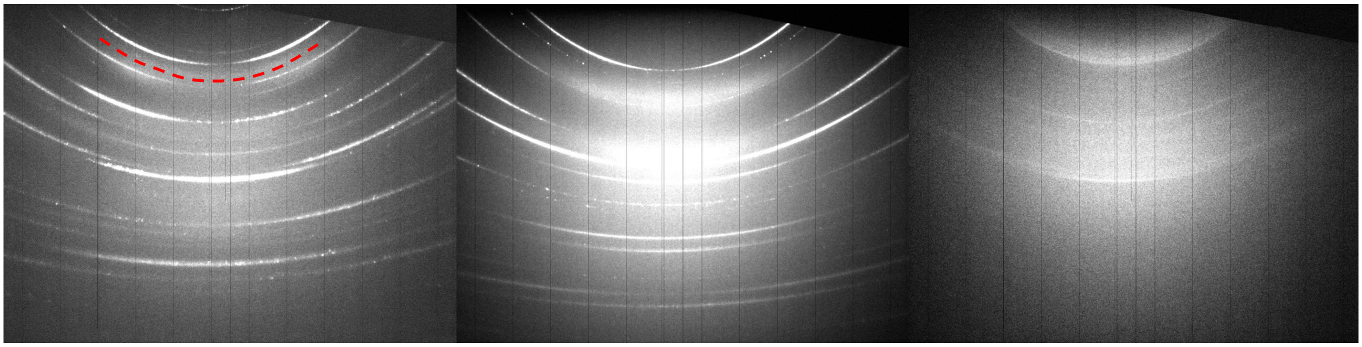

cr. + diffuse feat. (+amb. peaks)
SACLA 1 - 133(5) GPa

diffuse feat.(+amb. peaks)
SACLA 2 - 182(6) GPa

diffuse feat.
(+few amb. peaks)
SACLA 1 – Release 20-30 GPa

Figure S7. **2D diffraction image plate for data acquired in reflection.** 2D image plate of crystalline (cr.) Fe_2O_3 (remaining α'-Fe_2O_3 peak is shown in red dashed line) with amorphous Fe_2O_3 at 131(5) GPa (SACLA1 data), of liquid Fe_2O_3 at 182(6) GPa (SACLA2 data) and of a releasing non-crystalline phase after the release wave originating at the free-surface of the Fe_2O_3 layer reflects off the parylene-N-Fe_2O_3 interface and reaches the free surface again when the sample is probed leading to a pressure of 20-30 GPa (see section V of the Supplementary Material) (SACLA1 data), with remaining ambient (amb.) peaks. X-rays energy is 9.98 keV for SACLA1 and 9 keV for SACLA2. Angular range is 20 to 80° scattering angle and azimuthal range is 20 to 150°.

IV. BASELINE SUBTRACTION AND SMOOTHING OF INTEGRATED X-RAY DIFFRACTION PATTERNS

For all shots presenting no crystalline peaks (or very few) apart from the remaining ambient peaks we subtract the baseline using data on solid, crystalline Fe_2O_3 under shock at lower pressure. We also smooth the data prior to extracting structure factor and pair distribution function as detailed in the main paper. Details of different steps are shown in Fig. S8, Fig. S9 and Fig. S10.

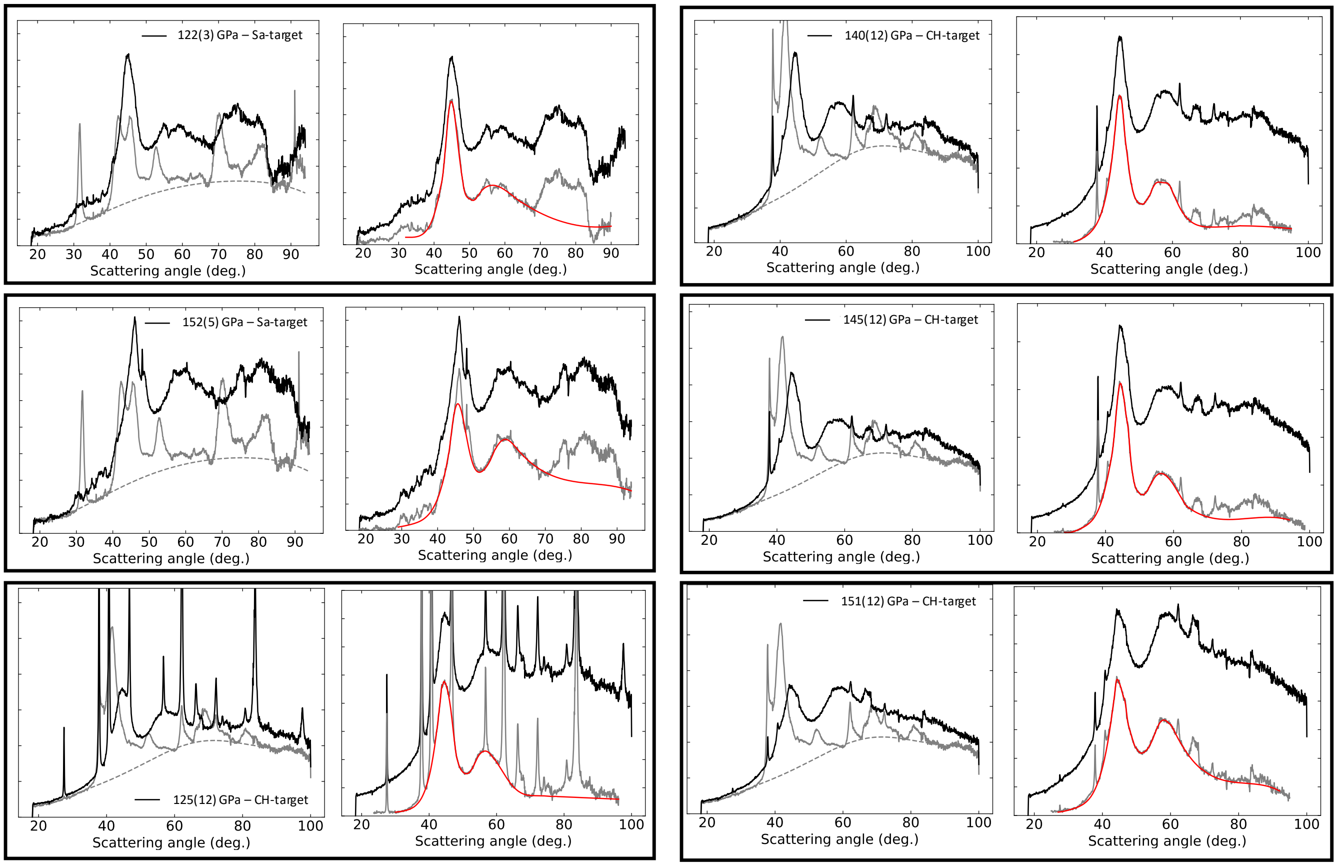

Figure S8. **Baseline subtraction for data acquired in transmission at 7.09 keV (LCLS data).** The baseline was evaluated from x-ray diffraction profile under shock on solid Fe_2O_3 at 116(3) GPa on CH-target for CH-targets data and at 81(2) GPa on Sa-targets for Sa-targets data. The baseline was adjusted (by multiplying by a factor) to match the signal at low angle where no amorphous/melt contribution is expected. On the left we show azimuthally integrated XRD profile of run under shock used for baseline after adjustment (grey), corresponding baseline (dashed grey) and XRD profile under shock (in black). On the right we show XRD profile under shock before (black) and after baseline removal (grey) and smoothing (in red). For Sa-target we can see that large sapphire signal and in some case integration artefact led to an ambiguous signal beyond 70 degrees, i.e. 4 Å^{-1}.

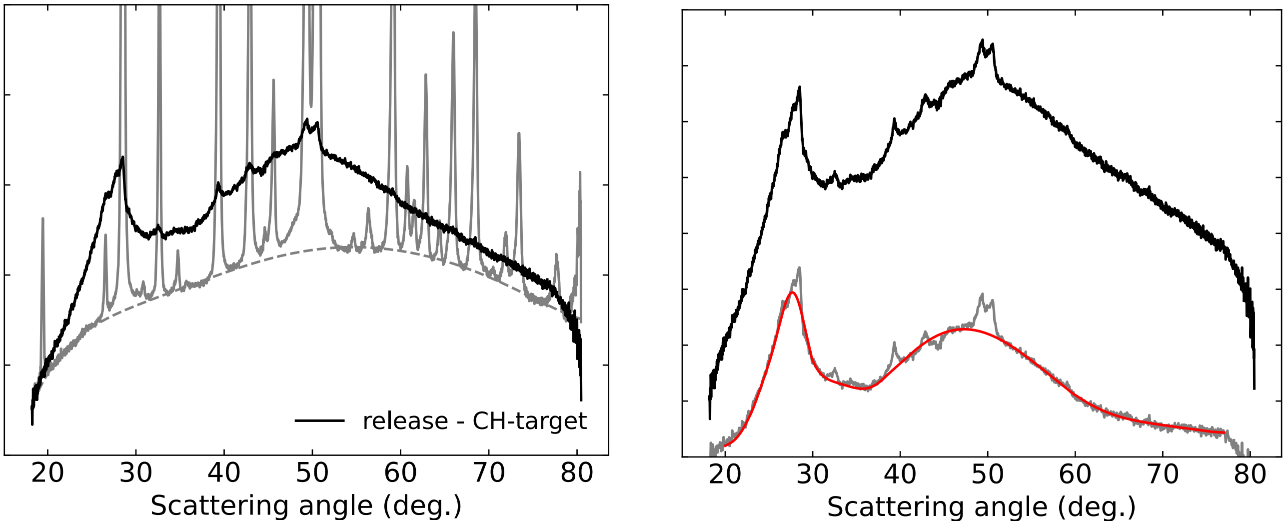

Figure S9. **Baseline subtraction for data acquired in reflection at 9.98 keV (SACLA1 data) upon release on CH-target.** The baseline was evaluated using x-ray diffraction pattern acquired on the same target prior to shock. The baseline was adjusted (shifted by + 10) to match the signal at low angle where no contribution from amorphous or melt is expected. On the left we show azimuthally integrated XRD profile of run under shock used for baseline after adjustment (grey), corresponding baseline (dashed grey) and XRD profile of amorphous/melt (in black). On the right we show XRD profile of the amorphous/melt phase (black) and XRD profile of the amorphous/melt after baseline removal (grey) and smoothing (in red). A similar approach was used to remove baseline for all release runs acquired in reflection (SACLA1 data) displayed in Fig. 3 of the main paper.

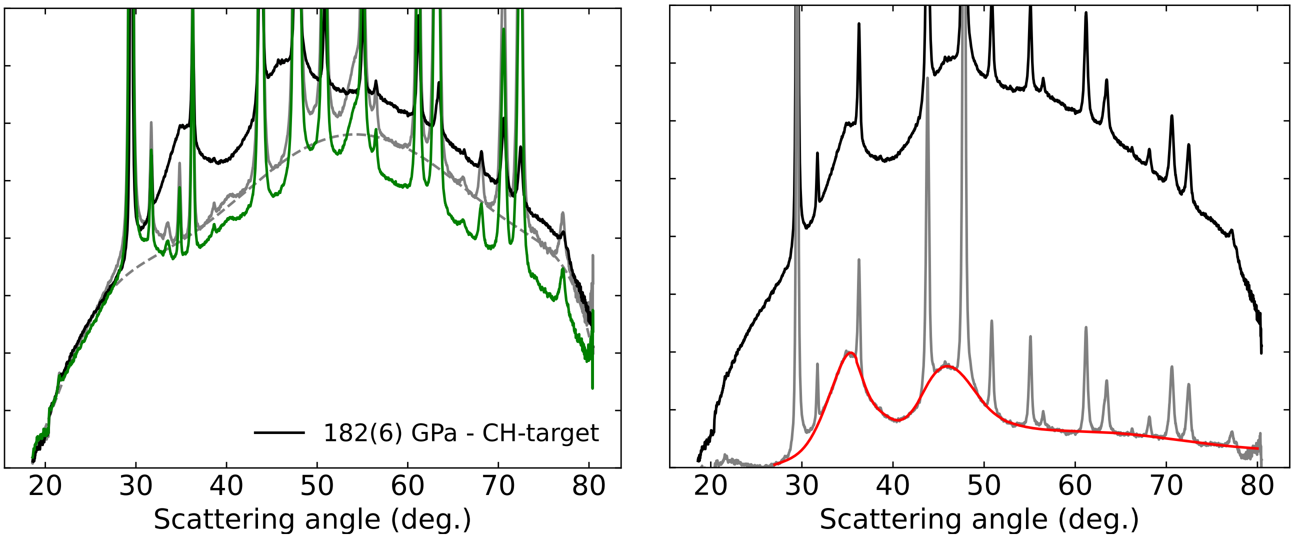

Figure S10. **Baseline subtraction for data acquired in reflection under shock at 9 keV (SACLA2 data) on CH-target.** The baseline was evaluated on XRD profile taken prior to shock as no suitable data under shock on solid Fe_2O_3 was available for this experiment. To account for plasma scattering under shock (contribution being likely to be small due to reflection geometry) we used an angle-dependent correction : exp(A x cos(2θ-x)) with 2θ the angle, and A and x two constants chosen to ensure that the baseline is as close as possible of the XRD profile of the melt at large angle similarly to what is observed for data acquired in transmission. The corresponding baseline was multiplied by a factor to match the melt signal at low angle (shifted by - 25) where no amorphous or melt contribution is expected. On the left we show azimuthally integrated XRD profile of run under shock used for baseline after adjustment (green), XRD profile of run under shock used for baseline after adjustment and additional angle-dependent correction (grey), corresponding baseline (dashed grey) and XRD profile under shock (in black). On the right we show XRD profile under shock before (black) and after baseline removal (grey) and smoothing (in red).

V. HYDRODYNAMIC SIMULATION FOR A SHOT PROBED UPON RELEASE 1.9 NS AFTER BREAKOUT

For one shot on a CH-target acquired in reflection geometry (SACLA1 data) and probed upon release, after a shock at 200(5) GPa, nearly no crystalline peak is observed in x-ray diffraction (see Fig. S9), 1.9 ns after the shock leaves the Fe_2O_3 layer. Hydrodynamic simulation performed with the code MULTI [4] displayed in Fig. S11 shows that the release wave originating at the free-surface of the Fe_2O_3 layer reflects off the parylene-N-Fe_2O_3 interface and reaches the free surface again at 1.9 ns after breakout, i.e. exactly when the sample is probed. As hydrodynamic calculations do not take into account the full range of release processes, an evaluation of the corresponding pressure was calculated based on the bond length shift observed on the pair distribution function, shown in Fig. 2 of the main paper, compared to the ambient pressure melt (as detailed in the main text).

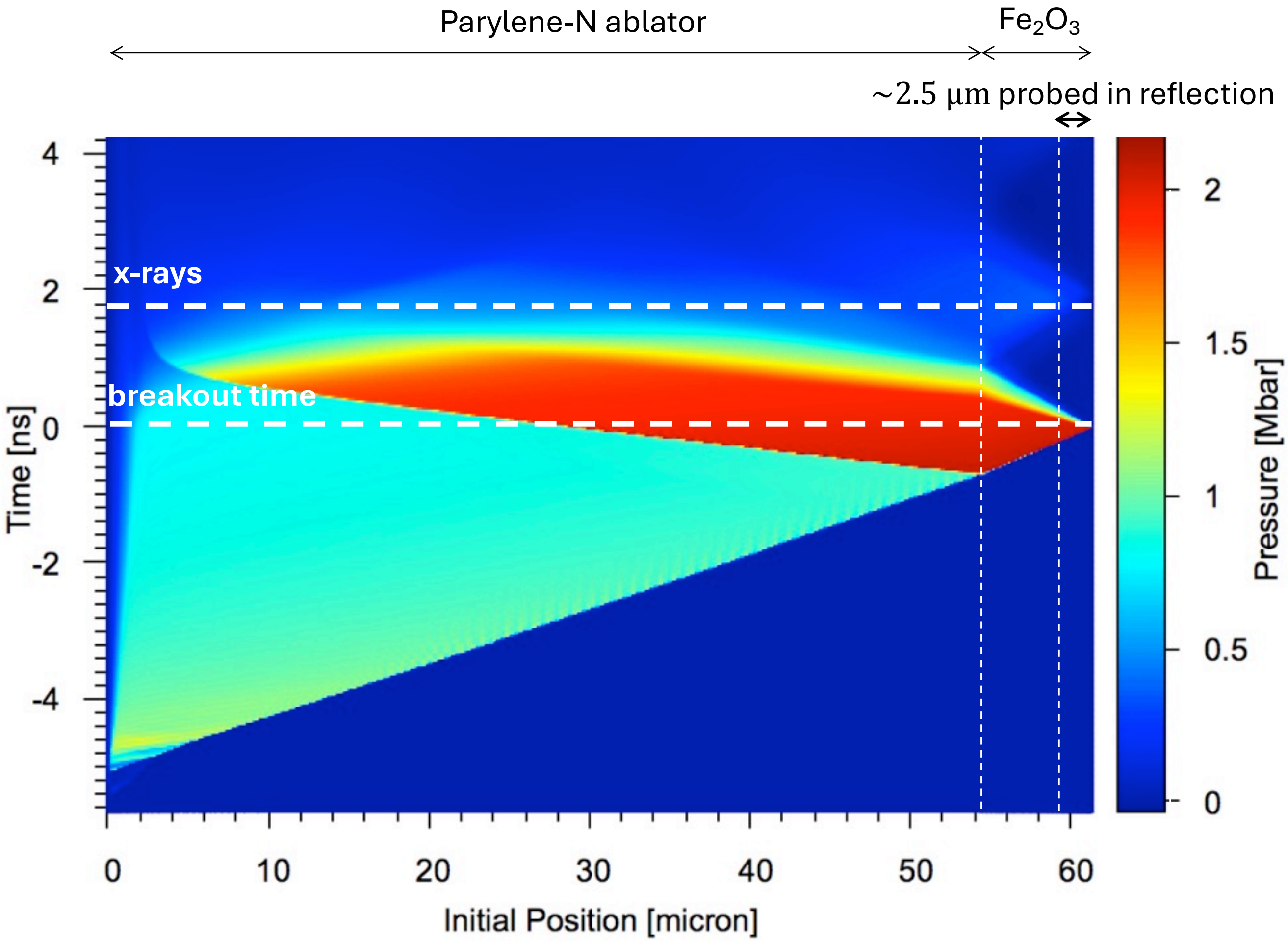

Figure S11. **Results of hydrodynamic calculation for Fe_2O_3 (CH-target) shocked at 200(5) GPa.**

VI. HYDRODYNAMIC SIMULATIONS FOR SA-TARGETS

For targets with a sapphire window, the Fe_2O_3 layer can be probed after the shock exits the sapphire window in order to measure an entirely compressed layer. This is the case for data points at 122(3), 152(5), 185(9) and 209(10) GPa. Indeed, the shock is maintained up to 1.5 ns after breakout time as shown in hydrodynamic simulations presented in Fig. S12. This is due to impedance matching between Fe_2O_3 and sapphire, as displayed in Fig. S13.

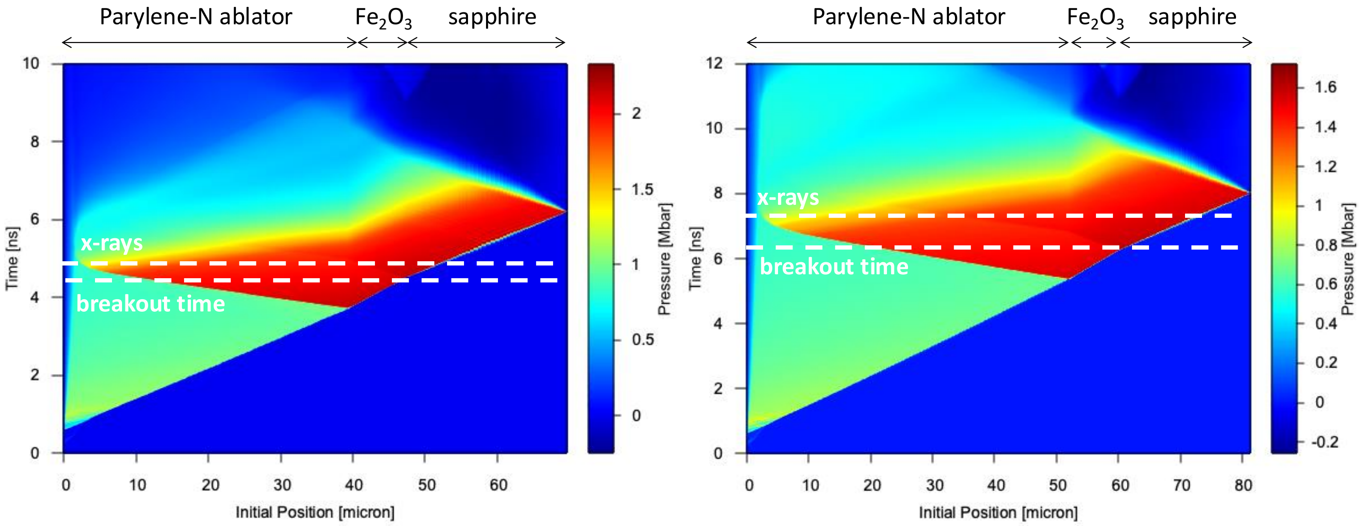

Figure S12. **Results of hydrodynamic calculation for Fe_2O_3 (Sa-targets) shocked at 152(5) and 209(10) GPa.** Hydrodynamic simulations performed with MULTI [4] for targets with a sapphire window in (left) reflection geometry (SACLA1), for data point at 209(10) GPa and in (right) transmission geometry (LCLS), for data point at 152(5) GPa. We can see that the shock is maintained up to slightly more than 1.5 ns after the shock exits the Fe_2O_3 layer.

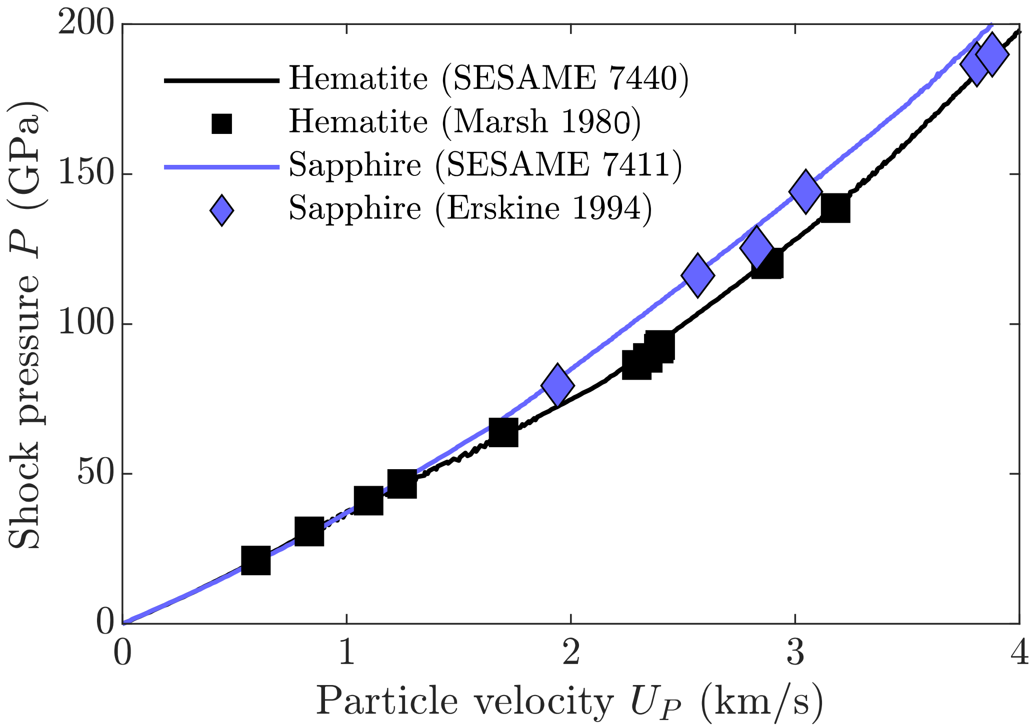

Figure S13. **Hugoniot relation for Fe_2O_3 (hematite) and sapphire based on SESAME equation of state 7440 and 7411 respectively [6].** Previous data under shock are shown for hematite [7] (high-explosive-driven experiments) and sapphire [8] (gas gun measurement).

VII. SUMMARY OF AMORPHOUS AND LIQUID DATA POINTS WITH DETAILED EVALUATION OF PEAKS POSITION

run	State	Laser intensity (W/cm^2)	Difference between set delay and breakout time (ns)	Pulse duration (ns)	Pressure (GPa)	Q1 (Å^{-1})	Q2 (Å^{-1})	Q1/Q2 intensity ratio	r1 (Å) Fe-O	r2 (Å)
FeO$_x$ 92% Fe^{3+} [9]	melt	-	-	-	0	2.40	4.20	1.20	1.92	3.30
SACLA1 CH-target	melt or amorphous	4.09e12	1.9	5	137(10) under shock ~20-30 for release	2.41	4.49	1.08	1.76	3.14
LCLS Sa-target	amorphous	3.25e12	0.2	10	122(3)	2.75	3.48	1.85	n.d.	n.d.
LCLS CH-target	amorphous	4.05e12	-0.8	10	125(12)	2.72	3.43	1.61	2.49	
SACLA1 CH-target	amorphous + α'	2.92e12	-0.3	5	131(5)	n.d.	n.d.	n.d.	n.d.	
SACLA1 CH-target	amorphous + α'	2.82e12	0	5	133(5)	n.d.	n.d.	n.d.	n.d.	
LCLS CH-target	amorphous	4.07e12	-0.3	10	140(12)	2.73	3.45§	1.84	2.56	
LCLS CH-target	amorphous	4.15e12	-0.4	10	145(12)	2.72	3.42	1.97	2.51	
LCLS CH-target	melt	8.33e12	-0.5	10	151(12)	2.78§	3.56§	1.07	2.16	
LCLS Sa-target	melt	4.35e12	1	10	152(5)	2.80	3.57	1.07	n.d.	n.d.
LCLS Sa-target	melt	5.06e12	-0.5	5	167(11)	2.76*	n.d.	n.d.	n.d.	n.d.
LCLS Sa-target	melt	5.09e12	-0.1	5	174(5)	2.75*	n.d.	n.d.	n.d.	n.d.
LCLS Sa-target	melt	5.11e12	-0.7	5	177(2)	2.79*	n.d.	n.d.	n.d.	n.d.
SACLA2 CH-target	melt	4.37e12	n.d.	5	182(6)	2.77	3.58	0.85	1.94 and 2.45	
LCLS Sa-target	melt	5.25e12	0.5	5	185(9)	2.77*	n.d.	n.d.	n.d.	n.d.
SACLA1 Sa-target	melt	5.0e12	0.4	5	209(10)	2.77*	n.d.	n.d.	n.d.	n.d.

Table I. **Summary of data points under shock and upon release showing nearly no crystalline phase (displayed in Fig. 1 and Fig. 2 of the main paper).** Set delay corresponds to the delay between the laser pulse and the XFEL probe, the breakout time (determined via VISAR analysis) corresponds to the moment when the shock exits the Fe_2O_3 layer. For SACLA2 experiment the set delay was not calibrated and timing of the probe compared to the breakout time could not be determined. Peaks positions (Q1 and Q2) and Q1/Q2 intensity ratio of the peaks are determined from structure factor displayed in Fig. 2 of the main paper and in some specified cases (*) from azimuthally integrated x-ray diffraction profile displayed in Fig. 1 of the main paper at the maxima of the peaks. For data point at 151(12) GPa the first and second peaks and for the data point at 140(12) GPa the second peak of the structure factor present a slight asymmetry due to remaining ambient peaks (visible in Fig. S8). In these cases (§) the position of the peak was evaluated by fitting a Gaussian to the peak and determining the maximum. Interatomic distances are given based on g(r) given in Fig. 2 of the main paper. For run under shock Fe-O and Fe-Fe contributions are overlapping in g(r) so we only give the observed maximum or maxima without assignation. For some data points it was not possible to assign a first peak position due to the presence of a remaining α'-Fe_2O_3 peak at the same position or a second peak position due to very high background linked to sapphire window or to extract the structure factor and pair distribution function for similar reason: in this case we left it as not determined (n.d.). For comparison ambient Fe_2O_3 melt is shown [9].

VIII. COMPARISON OF DFT+U CALCULATIONS AND SESAME 7440

P (GPa)	T(K) DFT+U alpha phase	T(K) DFT+U alpha prime phase	T(K) SESAME 7440	temperature difference (K)
1	294	-	323	-29
3	288	-	321	-34
4	282	-	320	-38
5	278	-	321	-42
7	276	-	322	-46
8	274	-	324	-49
10	274	-	326	-52
12	275	-	330	-55
13	278	-	335	-57
15	282	-	341	-58
17	288	-	347	-59
18	296	-	355	-59
20	305	-	363	-58
22	316	-	372	-56
24	329	-	382	-53
26	344	-	393	-48
28	361	-	404	-43
30	379	-	415	-36
33	399	-	427	-27
35	421	-	438	-17
37	444	-	449	-5
40	469	-	460	9
42	494	-	470	25
45	521	-	478	43
48	549	-	484	65
50	579	-	491	87
53	609	-	503	105
56	639	-	506	134
59	671	-	502	169
62	679	-	494	186
65	685	-	485	200
68	**-**	**800**	**480**	**320**
71	**-**	**863**	**483**	**381**
74	**-**	**918**	**498**	**420**
77	**-**	**973**	**531**	**442**
81	**-**	**1029**	**591**	**438**
84	**-**	**1085**	**656**	**429**
88	**-**	**1142**	**727**	**415**
91	**-**	**1200**	**803**	**397**
95	**-**	**1259**	**886**	**373**
99	**-**	**1319**	**975**	**344**
103	**-**	**1380**	**1071**	**309**
107	-	1443	1174	268
111	-	1507	1286	221
115	-	1573	1407	166
120	-	1641	1537	104

Table II. **Comparison between temperature (T) predicted by DFT+U calculations based on phases observed under shock [2] and SESAME 7440 [6].** Region of major discrepancies is evidenced in bold.

[1] R. L. Blake, R. E. Hessevick, T. Zoltai, and L. W. Finger, Refinement of the Hematite Structure, American Mineralogist **51**, 123 (1966).

[2] A. Amouretti, C. Crepisson, S. Azadi, D. Cabaret, T. Campbell, D. A. Chin, B. Colin, G. R. Collins, L. Crandall, G. Fiquet, A. Forte, T. Gawne, F. Guyot, P. Heighway, H. Lee, D. McGonegle, B. Nagler, J. Pintor, D. Polsin, G. Rousse, Y. Shi, E. Smith, J. S. Wark, S. M. Vinko, and M. Harmand, Phase transitions of Fe_2O_3 under laser shock compression 10.48550/arXiv.2402.18432 (2024).

[3] R. G. McQueen and S. P. Marsh, Handbook of Physical Constants (unpublished data), Geological Society of America Memoir **97**, 153 (1966).

[4] R. Ramis, J. M. ter Vehn, and J. Ramírez, Multi2d – a computer code for two-dimensional radiation hydrodynamics, Computer Physics Communications **180**, 977 (2009).

[5] Y. B. Zeldovitch and Y. P. Raizer, Shock waves in solids, in Physics of shock waves and high-temperature hydrodynamic phenomena, Elsevier , 685 (1967).

[6] J. Barnes and S. Lyon, SESAME: the Los Alamos National Laboratory equation of state database, Los Alamos National Laboratory (1987).

[7] S. Marsh, LASL shock Hugoniot data, University of California Press **5** (1980).

[8] D. Erskine, High pressure Hugoniot of sapphire, AIP Conf. Proc. **309**, 141 (1994).

[9] C. Shi, O. L. G. Alderman, A. Tamalonis, R. Weber, J. You, and C. J. Benmore, Redox-structure dependence of molten iron oxides, Communications Materials **1**, 80 (2020).